



Published in final edited form as:

*Nat Methods*. 2015 August ; 12(8): 736–738. doi:10.1038/nmeth.3449.

## Single cell magnetic imaging using a quantum diamond microscope

D. R. Glenn<sup>#1</sup>, K. Lee<sup>#2</sup>, H. Park<sup>3,4,5</sup>, R. Weissleder<sup>2,6</sup>, A. Yacoby<sup>3</sup>, M. D. Lukin<sup>3</sup>, H. Lee<sup>2</sup>, R. L. Walsworth<sup>1,3,5</sup>, and C. B. Connolly<sup>7</sup>

<sup>1</sup>Harvard-Smithsonian Center for Astrophysics, Cambridge, Massachusetts, USA

<sup>2</sup>Center for Systems Biology, Massachusetts General Hospital, Harvard Medical School, Boston, Massachusetts, USA

<sup>3</sup>Department of Physics, Harvard University, Cambridge, Massachusetts, USA

<sup>4</sup>Department of Chemistry and Chemical Biology, Harvard University, Cambridge, Massachusetts, USA

<sup>5</sup>Center for Brain Science, Harvard University, Cambridge, Massachusetts, USA

<sup>6</sup>Department of Systems Biology, Harvard Medical School, Boston, Massachusetts, USA

<sup>7</sup>Quantum Diamond Technologies, Inc., Somerville, MA, USA.

# These authors contributed equally to this work.

### Abstract

We apply a quantum diamond microscope to detection and imaging of immunomagnetically labeled cells. This instrument uses nitrogen-vacancy (NV) centers in diamond for correlated magnetic and fluorescence imaging. Our device provides single-cell resolution and two orders of magnitude larger field of view ( $\sim 1 \text{ mm}^2$ ) than previous NV imaging technologies, enabling practical applications. To illustrate, we quantify cancer biomarkers expressed by rare tumor cells in a large population of healthy cells.

---

Overcoming image degradation caused by autofluorescence and light scattering in complex media is a longstanding and important challenge in optical microscopy. Immunofluorescence imaging inevitably suffers from the admixture of the target signal with

---

Users may view, print, copy, and download text and data-mine the content in such documents, for the purposes of academic research, subject always to the full Conditions of use:[http://www.nature.com/authors/editorial\\_policies/license.html#terms](http://www.nature.com/authors/editorial_policies/license.html#terms)

Corresponding authors: hlee@mgh.harvard.edu, rwalsworth@cfa.harvard.edu, and cconnolly@quantumdiamondtech.com.

**Author Contributions:** D.R.G. and R.L.W. designed and constructed the quantum diamond microscope. C.B.C., H.L., and R.L.W. conceived the application of the quantum diamond microscope to the task of rare cell detection, and devised the experiments. K.L., R.W., and H.L. developed the optimal protocol for magnetic labeling of cells. K.L. prepared magnetic nanoagents, and carried out the cell labeling. D.R.G. and C.B.C. performed the experiments and analyzed the data. C.B.C., D.R.G., K.L., H.L., and R.L.W. wrote the manuscript, with discussion and input from all authors. A.Y., M.D.L., and R.L.W. conceived the application of NV diamond wide-field magnetic imaging to biomagnetism.

**Competing Financial Interests Statement:** M.D.L. and R.L.W. are co-founders of Quantum Diamond Technologies, Inc. (QDTI). M.D.L., R.L.W., and A.Y. all serve on the Scientific Advisory Board of QDTI and have financial interests in QDTI. R.W. has financial interest in T2Biosystems. R.W.'s interests are reviewed and managed by MGH and Partners HealthCare in accordance with their conflict of interest policies.

unwanted autofluorescence intrinsic to the sample, which cannot be completely removed by spectral filtering<sup>1</sup>. Furthermore, optical excitation and fluorescence collection are impeded by scattering and absorption in tissue or complex biofluids<sup>2</sup>, leading to reduced resolution in microscopy and degraded sensitivity in rapid detection modalities such as flow cytometry. A promising alternative approach is magnetic imaging of cells immunologically targeted with magnetic nanoparticles (MNPs), which can provide exceptional detection sensitivity owing to the low natural magnetic background in most biological samples<sup>3</sup>. Magnetic measurements of MNP-labeled cells have been realized with several existing technologies, including magnetoresistive sensors<sup>4,5</sup>, miniaturized NMR devices<sup>6,7</sup>, and Hall effect sensors<sup>8,9</sup>. To date, however, quantitative magnetic imaging of MNP-labeled biosamples under ambient conditions has not been possible with both single-cell resolution and scalability to macroscopic samples. Here, we report a promising solution to this problem using a new optical magnetic imaging modality known as the quantum diamond microscope<sup>10,11,12</sup>, which employs a transparent diamond chip sensor that is biocompatible<sup>13</sup> and easily integrated with standard microscope technology.

The quantum diamond microscope (**Fig. 1a**) employs a dense layer of fluorescent quantum sensors, based on nitrogen-vacancy (NV) color centers, near the surface of a diamond chip on which the sample of interest is placed. The electronic spins of the NV centers are coherently probed with microwaves, and optically initialized and read out to provide spatially resolved maps of local magnetic fields. The magnetic-field-dependent NV fluorescence occurs in parallel over the full ensemble of NVs at the diamond surface, resulting in a wide-field magnetic image with adjustable spatial pixel size set by the parameters of the imaging system. In principle, the number of independent magnetic detection channels for such a sensor is limited only by the number of available camera pixels and the sensor size relative to the optical diffraction limit, providing near-arbitrary image pixel size and field of view, with no intervening dead space.

To demonstrate the utility of the quantum diamond microscope for quantitative molecular imaging with single cell resolution, we configured the instrument for a particular task: rapid detection and magnetic imaging of a small number of cancer cells dispersed in a sample volume containing many background cells. The target cells were MNP-labeled to indicate the presence of antigens associated with circulating tumor cells (CTCs)<sup>14</sup>. To augment device performance for this application, we realized several important methodological advances over an earlier prototype applied to imaging of magnetotactic bacteria<sup>12</sup>. These included the use of an isotopically-enriched diamond substrate, the correction of lowest-order magnetic bias field inhomogeneity, and a significant suppression of technical noise. The instrumental upgrades yielded considerable improvement in the practical utility of the quantum diamond microscope, increasing the field of view by two orders of magnitude with no degradation in sensitivity compared to the earlier device.

We first verified the NV-diamond magnetic imaging protocol using model samples prepared by magnetically labeling cancer cells (SKBR3) with HER2-specific MNPs (**Fig. 1b-c**). MNP-labeled cells were further stained with fluorescent dye (carboxyfluorescein succinimidyl ester/CFSE) to enable cell identification by *in situ* fluorescence. A solution containing a mixture of labeled and un-labeled cells was placed on the diamond surface, and

then a series of correlated brightfield, fluorescence, and magnetic images were acquired using a field of view of 1 mm × 0.6 mm. Comparison of bright-field and fluorescence images (**Fig. 2a**) to magnetic images (**Fig. 2b**) verified that all MNP-labeled cells were detected with good signal-to-noise ratio (SNR) while all un-labeled cells were rejected in less than 1 minute of magnetic signal acquisition. For example, in a typical field of view (**Fig. 2a-b**), every one of 86 labeled cells (as identified by fluorescence) in a total sample of 436 cells also produced a detectable magnetic field signature. The characteristic two-lobed magnetic field pattern produced by the MNP-labeled cells matched well with models assuming a roughly spherical distribution of magnetic dipoles (**Fig. 1c** and **Supplementary Note 1**). This pattern could be reliably fit to an analytic function to extract the peak magnetic field magnitude, which we refer to here as the magnetic signal. The procedure was effective even in cases where the spatial extent of the magnetic dipole field pattern exceeded the distance between adjacent labeled cells (**Supplementary Note 2**). For cells displaying relatively strong expression of the labeled antigen (such as the HER2 biomarker on the SKBR3 cell line shown), we observed magnetic signals on the order of 3 μT, compared to a noise floor of ~200 nT under these imaging conditions.

We next performed a titration measurement to assess the fidelity of the quantum diamond microscope for rare cell detection. Samples of SKBR3 cells were labeled with HER2-specific MNPs, and were then mixed in the appropriate volumetric ratios with samples of otherwise identical un-labeled cells to produce mixtures with known labeled fractions. Each mixture was then repeatedly measured in bright-field and magnetic imaging modes, and the fraction of cells producing magnetic field signatures above the detection threshold was tabulated. The rate of magnetic cell detection for each sample corresponded well with the expected fraction of labeled cells based on the mixing ratios (**Fig. 2c**), indicating a high fidelity of successful detection.

We further evaluated the quantum diamond microscope's ability to quantify biomarker expression by detecting MNP-labeled cells across a range of cell lines using different target antigens. Samples of cells from three breast cancer lines (SKBR3, MCF7, MDA-MB-231) were individually incubated with one of three separate MNP preparations, each targeting a different putative cancer biomarker (EGFR, EpCAM, HER2), for a total of nine cell/biomarker combinations. Each sample was magnetically imaged over multiple fields of view, and histograms of the magnetic signals associated with each cell/biomarker combination were accumulated (**Fig. 2d-e**). In parallel, cells from the same lines were alternatively labeled with fluorescent antibodies, and marker expressions were measured by fluorescence flow cytometry (FC). The distribution widths for magnetic detection were comparable to those in the FC data, indicating that magnetic detection had not introduced extra fluctuations in signal intensity above the natural variability in biomarker expression. Furthermore, comparison of the two measurements showed strong correlation of the mean magnetic signals with mean FC fluorescence intensity (Pearson coefficient  $r = 0.985$ ; **Fig. 2f**), validating the utility of the quantum diamond microscope as a quantitative imaging platform.

The quantum diamond microscope uses NV centers in diamond to obtain co-registered optical and magnetic images of targets labeled with MNPs. The results presented here

demonstrate rapid imaging of magnetic fields over a  $\sim 1 \text{ mm}^2$  field of view, enabling unambiguous detection of magnetically-labeled cells. More generally, this technology provides dynamically reconfigurable (cellular or sub-cellular) magnetic imaging with resolution down to the optical diffraction limit (**Supplementary Note 3**), over a continuous and transparent sensing surface suitable for integration with multiplexed optical microscopy. The superparamagnetic MNPs used for labeling bind reliably to provide a strong additive magnetic signal, facilitating quantitation of biomarker expression with negligible magnetic background and straightforward sample preparation. Furthermore, the technique is intrinsically robust to complex sample media: the spectrally narrow NV spin resonance used to determine optically the magnetic field is unaffected by other fluorescent sources; green light used for NV excitation is constrained to pass through the side faces of the diamond chip by total internal reflection, thereby protecting the sample from unwanted optical interactions; and the NV fluorescence can be collected through the back face of the diamond without interacting with an optically active or obscuring sample such as blood (**Supplementary Note 4**). The unique combination of features provided by the quantum diamond microscope can now be used to address a range of interesting problems, including those that involve other immunomagnetically labeled targets, such as pathogen detection or the molecular profiling of microvesicles. Other processes can also be associated with magnetic signatures to enable: (i) study of the cellular uptake of magnetic nanoparticles with different surface chemistry; and (ii) precise measurements of the differential accumulation of nanoparticles among widely varying cell types (e.g., cancer cells vs. macrophages).

## Online Methods

### Magnetic imaging by optically detected magnetic resonance (ODMR)

The negatively charged NV color center is a stable point quantum defect in diamond, consisting of a substitutional nitrogen adjacent to a vacancy in the lattice. In the  $S=1$  electronic ground state, the  $m_s = 0$  and  $m_s = \pm 1$  spin projection sublevels are split by approximately 2.87 GHz at zero magnetic field. Spin-state-dependent decay from the excited triplet electronic state to metastable singlet states allows optical polarization into the  $m_s=0$  state, as well as fluorescent readout of the NV spin state<sup>15</sup>. The projection of the local magnetic field,  $B$ , along the NV axis is determined by measuring the Zeeman-induced splitting of these sublevels ( $\Delta E = \gamma B$ , for NV gyromagnetic ratio  $\gamma = 2.8 \text{ MHz/gauss}$ ) using coherent microwave manipulation. A straightforward implementation of static-field magnetometry with NV centers, employed in the present work, uses optically detected magnetic resonance (ODMR), in which green light at 532 nm continuously drives the NV electronic transition while a continuous-wave microwave source is scanned near one of the  $m_s=0 \rightarrow m_s=\pm 1$  ground state spin transitions, and the resulting Stokes-shifted fluorescence from the NV center or NV ensemble is monitored. When the microwave drive comes into resonance with the Zeeman-shifted NV spin transition, the steady-state NV population in the  $m_s=0$  ground state is reduced, resulting in a detectable decrease in fluorescence due to temporary NV shelving in the metastable singlet state. The magnetic field sensitivity is determined by the precision of the ODMR frequency measurement, given roughly by the resonance linewidth divided by the fluorescence signal-to-noise ratio. With a bias magnetic field ( $B_0 \approx 400 \text{ Gauss}$ ) aligned along one of the four possible NV axes (i.e., a [111] axis in

the diamond lattice), the ensemble of NV centers aligned with that ‘sensor’ axis is spectrally distinguishable from the other three (degenerate) NV orientation classes. At the diamond chip’s magnetic imaging surface, spatial variations of the magnetic field projection along the sensor direction induce local Zeeman shifts in NV spin transition frequencies<sup>11</sup>. ODMR is performed simultaneously on the  $m_s = 0 \rightarrow m_s = +1$  and  $m_s = 0 \rightarrow m_s = -1$  transitions to correct for possible systematic effects due to internal strain in the diamond<sup>15</sup>.

### NV-diamond magnetic imaging system

Magnetic field images were acquired by spectroscopic interrogation of NV centers near the surface of a synthetic monocrystalline diamond chip (2 mm × 2 mm × 0.5 mm). The diamond was grown using chemical vapor deposition (CVD) by Element Six, Ltd., with highpurity precursor gases to limit <sup>13</sup>C concentration to <10<sup>-5</sup>. (This concentration, well below the natural abundance of ~10<sup>2</sup>, significantly reduces the effect of interactions with spin- 1/2 <sup>13</sup>C nuclei in the vicinity of the NV centers.) The diamond was implanted with <sup>14</sup>N<sup>+</sup> ions at 14 keV beam energy, resulting in a highly-enriched layer of nitrogen ~10 nm thick at a mean depth of ~20 nm below the surface (estimated using Stopping and Range of Ions in Matter [SRIM] software). Vacuum annealing was carried out to efficiently convert implanted <sup>14</sup>N and vacancies into NV centers in the following sequence: ramp from room temperature to 400°C over 2 hours, then hold for 2 hours; ramp 400°C to 800°C over 2 hours, then hold for 8 hours; ramp 800°C to 1,100°C over 2 hours, then hold for 3 hours. The estimated final NV density in the surface layer was 3 × 10<sup>11</sup>/cm<sup>2</sup> and the measured ODMR linewidth of each NV hyperfine transition was approximately 600 kHz FWHM. We note that a number of technical improvements related to diamond chip fabrication, microwave delivery and MNP labeling procedures will significantly increase the sensitivity and utility of a next generation device (**Supplementary Note 5**).

Samples to be imaged (fixed, MNP-labeled cells in buffer solution or blood, as described below) were applied directly to the diamond surface with the shallow NV layer. Light from a diode-pumped solid state laser (Coherent Verdi) at 532 nm was directed into the bottom of the diamond chip through a glass cube, to which the diamond was affixed with a thin layer of optical adhesive (Norland NBA107). The angle of incidence was chosen to be below the critical angle for total internal reflection within the diamond at the surface with the NV layer, so that none of the laser light could propagate out from the diamond surface and through the sample. The laser spot size could be varied up to a maximum of approximately 1 mm × 0.6 mm, with an estimated average intensity of approximately 30 W/cm<sup>2</sup>. NV fluorescence was collected using a home-built microscope consisting of an objective (Zeiss Plan Achromat, 20×/0.8), an interference filter (Semrock LP02-633RU), a tube lens (ThorlabsAC254-100-B-ML), and a sCMOS camera (Andor Neo). The tube lens had focal length  $f=10$  cm, chosen to halve the standard magnification of the objective (approximately), at the expense of slight image distortion near the edges of the field of view. Camera exposures were 25 ms in duration for each microwave frequency step. The microwave ODMR signal was provided by a low noise synthesizer (Agilent E4428C) with sweeps over the  $m_s=0 \rightarrow m_s=-1$  (frequency  $f_0 \approx 1.64$  GHz) and  $m_s=0 \rightarrow m_s=+1$  ( $f_0 \approx 4.09$  GHz) resonances interleaved point by point. A switch (Mini-Circuits ZASWA-2-50DR) was used to alternate between two amplifiers (Mini-Circuits ZHL-10W-2G and ZHL-16W-43-S) in

the appropriate frequency bands for each resonance, and the output microwave signal was applied to the diamond and NV spins through a pair of small (~200  $\mu\text{m}$  diameter), closely spaced wires. The entire experiment was controlled using home-built Matlab software, with a programmable TTL pulse generator (Spincore Pulseblaster) used to synchronize switches and other hardware.

### Magnetic image analysis

Analysis of ODMR fluorescence data for characterization of NV-based MNP-labeled cell detection was carried out in two parts: (i) fitting of raw ODMR data to extract pixel-wise magnetic resonance lineshapes, from which local magnetic field strengths could be determined; and (ii) processing of wide-field magnetic images and correlated bright-field and/or fluorescence images to determine the positions and intensities of magnetic signals from labeled cells. Pixel-by-pixel fitting was performed on the ODMR fluorescence images acquired directly from the camera, sometimes with additional binning to average spectra in adjacent pixels for improved SNR. (For the image shown in **Fig. 2b**, binning was  $3 \times 3$  in hardware and  $2 \times 2$  in software, resulting in a total binned image pixel size of  $3.5 \mu\text{m}$ .) In each binned pixel, a sum of three Lorentzian lineshapes was fit to the fluorescence intensity as a function of microwave frequency, with the frequency splitting between the peaks fixed to the known  $^{14}\text{N}$  longitudinal hyperfine splitting of 2.2 MHz in NV centers<sup>16</sup>. This fit was carried out independently for the  $m_s=0 \rightarrow m_s=-1$  and  $m_s=0 \rightarrow m_s=+1$  transitions. Each NV hyperfine triplet was fit with a single variable linewidth parameter and three variable amplitudes, to account for variations over the field of view in microwave drive power and  $^{14}\text{N}$  nuclear polarization<sup>17</sup>, respectively. A single frequency parameter was fit to the central resonance frequency of each hyperfine triplet, and the difference in frequencies for the two transitions was calculated to determine the local magnetic field projection in the pixel:  $B = (f_{0 \rightarrow +1} - f_{0 \rightarrow -1})/2\gamma$ , for the NV gyromagnetic ratio  $\gamma = 2.8 \text{ MHz/Gauss}$ . Finally, a quadratic background subtraction was performed over the full magnetic image to remove the effect of bias field inhomogeneity (typically about  $10^{-3}$  of the mean bias field value over a  $\sim 1 \text{ mm}^2$  field of view). The processed magnetic image was displayed using the default 64-color 'jet' colormap lookup table in Matlab.

The full magnetic image was then compared to spatially correlated bright-field and/or fluorescence images to characterize the magnetic labeling of the sample cells. Cell locations were determined using an automated circle-finding algorithm (circular Hough), and the image was segmented into regions containing clusters of contiguous cells. A twodimensional fit function was constructed from the cell locations, consisting of one approximate "dipole" pattern for each cell in the cluster. Dipoles were modeled by the product of a Gaussian function in the vertical direction and the first derivative of a Gaussian in the horizontal direction; the spatial centers of each such dipole were fixed relative to each other to correspond to the relative cell positions, but the overall center of the pattern was allowed to vary. Widths of the Gaussian and Gaussian derivative functions were also fixed, and the amplitude of each dipole was left as a free parameter. The list of leastsquares fit dipole amplitudes for each cell-cluster sub-image was recorded, and histograms of dipole intensities accumulated as shown (**Fig. 2d-f**) in the main text. We determined an imaging noise floor of approximately 200 nT by applying our image processing and signal fitting

procedures to a set of 1,000 images of randomly-generated noise. This noise was chosen to have the same magnitude and spatial scale as that measured in images with no cell sample present.

### Cell lines

The following cell lines were purchased from the American Type Culture Collection (ATCC): SKBR3, MCF7 and MDA-MB-231. All cell lines were mycoplasma-tested and authenticated by the vendor. The cells were cultured in Dulbecco's modified Eagle's medium (Cellgro) or RPMI 1640 (Cellgro) medium supplemented with fetal bovine serum (FBS, Cellgro, 10%), penicillin and streptomycin (Cellgro, 1%), and L-glutamine (1%). Cell lines were cultured at 37°C in a humidified atmosphere containing 5% CO<sub>2</sub>. At their 70% confluence, cells were washed with phosphate buffered saline (PBS), trypsinized, and resuspended in PBS solution containing 2% FBS and 1% BSA (C-PBS). Approximately  $1.5 \times 10^5$  cells were prepared for each experiment and incubated them in C-PBS containing antibodies functionalized with magnetic nanoparticles (100 µg [Fe]/mL).

### Antibody preparation

Cells were magnetically labeled through biotin–streptavidin chemistry, targeting three different antigens: human epidermal growth factor receptor 2 (HER2)/*neu*, epidermal growth factor receptor (EGFR), and epithelial cell adhesion molecule (EpCAM). The following monoclonal antibodies were biotinylated for conjugation with streptavidincoated MNPs: anti-HER2/*neu* (trastuzumab, Genentech), anti-EGFR (cetuximab, Imclone Systems), and anti-EpCAM (MAB9601, R&D Systems). Antibodies were purified by Zeba column (Thermo Scientific), and subsequently incubated with sulfosuccinimidyl-6-[biotinamido] hexanoate (Sulfo-NHS-LC-Biotin solution, Thermo Scientific) overnight at 4° C. Biotinylated antibodies were then purified by Zeba column to remove excess reagents. Antibody concentrations were determined by absorbance measurements.

### Cell labeling

Cells in suspension were incubated with biotinylated antibodies for 20 min at room temperature. Excess antibodies were removed via centrifugation (1,500rpm, 2 min). Streptavidin-coated superparamagnetic MNPs (Ocean Nanotech, 20-nm magnetite core) in C-PBS were then introduced, and the mixture was incubated for 20 min at room temperature. Excess MNPs were removed by centrifugation, and the MNP-labeled cells were further fixed using a fixation kit (phosflow, BD Scientific). For the separate fluorescent identification, the MNP-labeled cells were further stained CFSE (CellTrace™ CFSE Cell Proliferation Kit, Molecular probes) according to the vendor-recommended protocol.

### Flow cytometry measurement

Flow cytometry was used for validation of biomarker expression levels in each cell line. Antibodies were pre-conjugated with fluorophore (FITC) prior to cell labeling. Target cells were incubated with antibodies in C-PBS for 20 min at room temperature. The flow cytometry fluorescence measurements were performed using a LSR II flow cytometer

(Becton Dickinson), and mean fluorescence intensity was determined using FlowJo software.

## Supplementary Material

Refer to Web version on PubMed Central for supplementary material.

## Acknowledgements

The authors thank M.L. Mckee for help with electron microscopy, as well as M. Liong and H. Shao for advice on magnetic assay protocols. This work was supported in part by NIH Grants R01HL113156 (H.L.) and U54-CA119349 (R.W.), as well as the DARPA QuASAR program, and DARPA SBIR contract W31P4Q-13-C-0064.

## References

1. Billinton N, Knight AW. *Analytical biochemistry*. 2001; 291:175–197. [PubMed: 11401292]
2. Visser TD, Groen FCA, Brakenhoff G, J. *Journal of Microscopy*. 1991; 163:189–200.
3. Issadore D, et al. *Lab on a Chip*. 2014; 14:2385–2397. [PubMed: 24887807]
4. Osterfeld SJ, et al. *Proceedings of the National Academy of Sciences*. 2008; 105:20637–20640.
5. Gaster RS, et al. *Nature medicine*. 2009; 15:1327–1332.
6. Lee H, Sun E, Ham D, Weissleder R. *Nature medicine*. 2008; 14:869–874.
7. Lee H, Yoon T-J, Figueiredo J-L, Swirski FK, Weissleder R. *Proceedings of the National Academy of Sciences*. 2009; 106:12459–12464.
8. Issadore D, et al. *Science translational medicine* 4. 2012:141ra92.
9. Gambini S, Skucha K, Liu PP, Kim J, Krigel R. *IEEE Journal of Solid-State Circuits*. 2013; 48:302–317.
10. Taylor JM, et al. *Nature Physics*. 2008; 4:810–816.
11. Pham LM, et al. *New Journal of Physics*. 2011; 13:045021.
12. Le Sage D, et al. *Nature*. 2013; 496:486–489. [PubMed: 23619694]
13. Tang L, Tsai C, Gerberich WW, Kruckeberg L, Kania DR. *Biomaterials*. 1995; 16:483–488. [PubMed: 7654876]
14. Yu M, Stott S, Toner M, Maheswaran S, Haber DA. *The Journal of cell biology*. 2011; 192:373–382. [PubMed: 21300848]
15. Doherty MW, et al. *Physics Reports*. 2013; 528:1–45.
16. Felton S, et al. *Physical Review B*. 2009; 79:075203.
17. Fischer R, Jarmola A, Kehayias P, Budker D. *Physical Review B*. 2013; 87:125207.



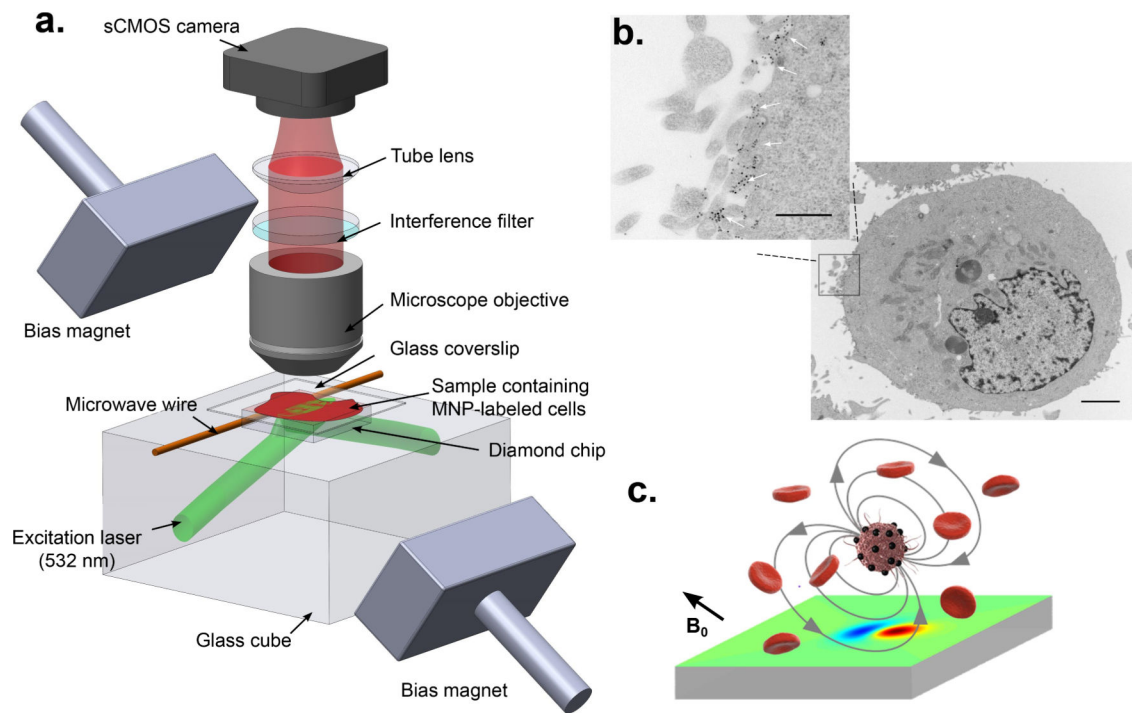


**Figure 1. Quantum diamond microscope for magnetically-labeled targets**

(a) Wide-field NV diamond magnetic imaging microscope. Samples containing immunomagnetically-labeled cells are placed directly on the surface of a diamond chip with a highly enriched surface layer of NV centers. NV electronic spins are probed by optically detected magnetic resonance (ODMR) using 532 nm laser light and microwaves, with NV fluorescence imaged onto a sCMOS camera. For each imaging pixel this procedure determines the magnetic field projection along one of the [111] diamond axes over a  $1 \text{ mm} \times 0.6 \text{ mm}$  field of view. (Diagram adapted from previous work<sup>12</sup>.) (b) Electron micrograph of a SKBr3 cell labeled with magnetic nanoparticles (MNPs) conjugated to HER2 antibodies. Expanded view: MNPs are visible as black dots on the cell membrane (indicated by white arrows). Scale bars are  $2 \mu\text{m}$  in main figure,  $500 \text{ nm}$  in inset. (c) Diagram of an MNP-labeled target cell above the diamond surface, surrounded by unlabeled normal blood cells. MNP labels are magnetized by the externally-applied magnetic bias field  $B_0$ , which is aligned as shown with the diamond [111] axis. The magnetic field produced by the MNPs is imaged using the shallow NV layer near the diamond surface to produce the characteristic dipole-like pattern shown (distorted here for perspective).

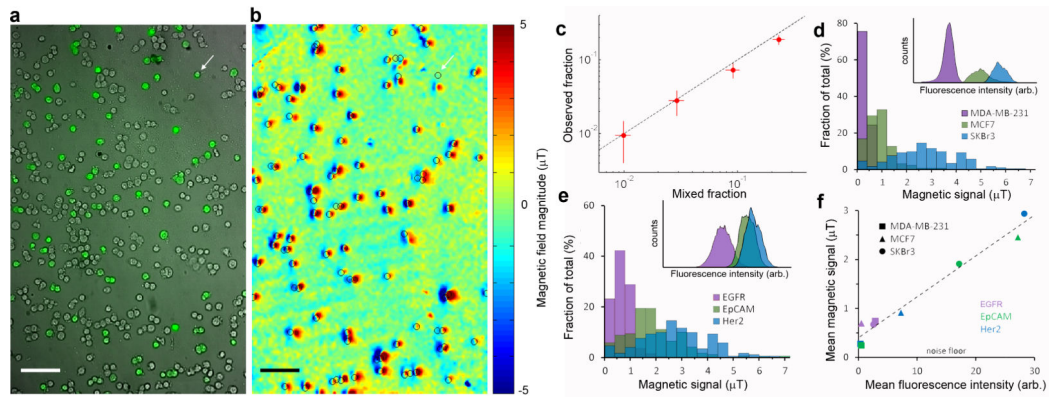


**Figure 2. Wide-field imaging for quantitative magnetic measurement of biomarker expression on multiple cell lines**

(a) Co-localized bright field and fluorescence images of a mixture of two subsamples of SKBR3 cells, where one subsample has been magnetically labeled with magnetic nanoparticles (MNPs) conjugated to HER2 antibodies and stained with fluorescent dye. The fluorescence overlay identifies the MNP-labeled cells. (b) Magnetic field image of the same field of view shown in a, with all magnetically-labeled cells producing characteristic dipolelike patterns. One cell (white arrow) moved during acquisition; otherwise the detection rate is 100%. Scale bars: 100  $\mu\text{m}$ . (Images a and b are representative of three sets of correlated images taken of the same sample under these conditions.) (c) Measured fraction of imaged cells producing magnetic signal  $>1 \mu\text{T}$  as a function of the mixed fraction of labeled cells. Correspondence indicates good detection fidelity. Error bars are Poissonian standard deviations ( $N > 200$  at each point). (d) Histogram of magnetic signals for three cancer cell lines, labeled by MNPs conjugated to anti-HER2. Inset shows flow cytometry (FC) fluorescence intensity distributions (logarithmic horizontal axis) for different samples of the same cell cultures, labeled by anti-HER2-conjugated fluorophores. (e) Histogram of magnetic signals for three samples of SKBR3 cells labeled with MNPs conjugated to antibodies for three different common CTC biomarkers. Inset shows comparison FC data, as in d. (f) Measured magnetic distribution means vs. flow cytometry fluorescence distribution means for all nine cell/biomarker combinations. Linear correspondence ( $r = 0.985$ ) shows that the magnetic signal reliably quantifies biomarker expression.